Appl Phys B (2010) 100: 189–194
DOI 10.1007/s00340-010-3994-x

Applied Physics B
Lasers and Optics

Near-infrared resonant photoacoustic gas measurement using simultaneous dual-frequency excitation

J.M. Rey · C. Romer · M. Gianella · M.W. Sigrist

Received: 4 March 2010 / Published online: 26 March 2010

Abstract The simultaneous dual-frequency operation of a resonant photoacoustic gas sensor based on the differential mode excitation photoacoustic (DME-PA) technique is presented. The DME-PA method uses the excitation of two different modes in a resonant photoacoustic cell and the gas concentration is derived from the amplitude ratio of these acoustic modes. With the simultaneous dual-frequency excitation, the amplitude ratio needed by the DME-PA technique is obtained instantaneously, in contrast to the sequential modulation scheme where additional time delays are introduced by changing the modulation frequency. For a given excitation power reaching the photoacoustic cell, and a total acquisition time longer than 7 s, the simultaneous modulation scheme provides an improved measurement uncertainty compared to the sequential scheme. The proposed sensor allows measuring water vapour with a ±150 ppmV uncertainty using current-modulated near-infrared LEDs and a 15 s total acquisition time.

1 Introduction

Gas sensors based on the photoacoustic effect allow direct measurement of the light absorbed by the sample and thus present high sensitivity and large dynamic range [1–5]. The photoacoustic effect consists of conversion of absorbed light energy into acoustical waves, which can be detected with a sound pickup device (e.g. a microphone). Different designs for photoacoustic cells have been proposed: acoustically resonant [4–10], multipass [11, 12], intracavity [13, 14], parallel [15], "windowless" [16], differential [17] and quartz enhanced [18]. In most known photoacoustic sensing schemes, the absolute values of the microphone signal are measured and used to derive the concentration of the gas of interest ([3] and references therein). Since photoacoustic signals depend on the intensity of the excitation light source, some kind of intensity normalisation schemes (e.g. power meter or reference cells) are required for quantitative measurements. Such normalisation schemes reduce the susceptibility to intensity fluctuations of the light source, but the resulting gas concentration is still sensitive to microphone, power meter as well as electronic noise and drift.

To reduce the complexity associated with the required normalisation scheme, a photoacoustic gas sensor based on a photoacoustic scheme named differential mode excitation photoacoustic (DME-PA) spectroscopy has been proposed [19]. The DME-photoacoustic method is based on the selective excitation of two different modes in a resonant photoacoustic cell and the gas concentration is derived from the amplitude ratio of these acoustic modes. The DME-PA technique also reduces the impact of microphone and electronics drifts on the measured gas concentration. Simultaneous amplitude modulation of a heated black-body infrared light source with two choppers at different frequencies allowed the determination of acetone vapour concentrations without changing the chopper modulation frequency [20]. The simultaneous acquisition of signals at both resonance frequencies with the dual-modulation scheme reduces drifts on the timescale needed to obtain the photoacoustic amplitude ratio.

Based on the DME-PA technique, a gas sensor for water vapour has recently been presented [21]. A current-modulated near-infrared light emitting diode (LED) was

J.M. Rey · C. Romer · M. Gianella · M.W. Sigrist (✉)
Laser Spectroscopy and Sensing Laboratory, Institute of Quantum Electronics, ETH Zurich, Schafmattstr. 16, 8093 Zurich, Switzerland
e-mail: sigrist@iqe.phys.ethz.ch
Fax: +41-1-6331230

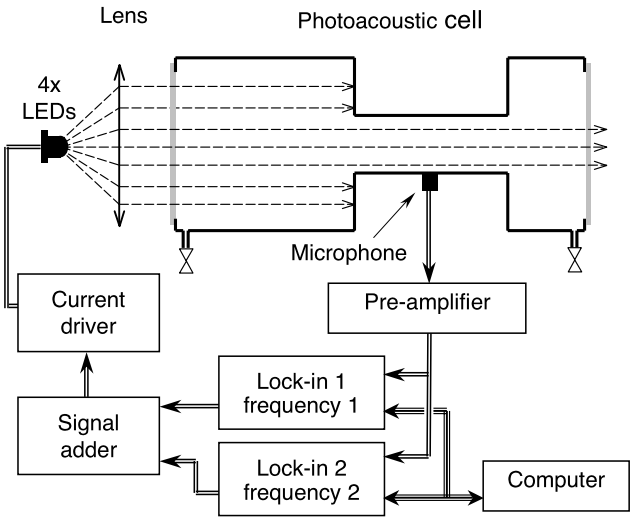

Fig. 1 Schematic representation of the photoacoustic arrangement used in this work

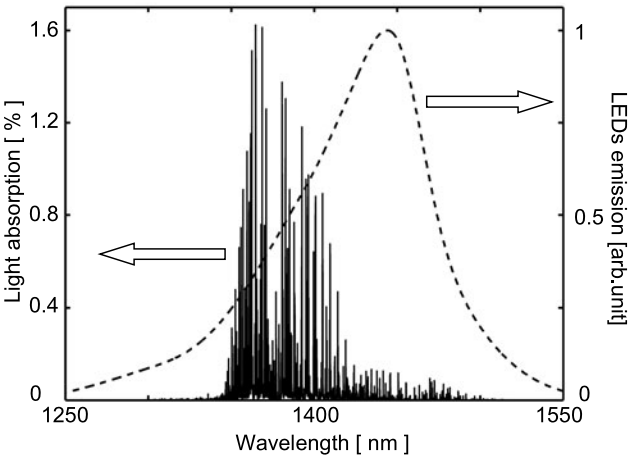

Fig. 2 Absorption spectrum (*full line*) of water vapour (1%vv, 980 mbar, 295 K, absorption pathlength = 1 cm) from the HITRAN database [30]. The *dashed line* shows the emission spectrum of the InGaAsP near-infrared LEDs used in this work

used as excitation source around 1400 nm. In addition to the excellent stability, this sensor is robust since it contains no moving parts.

This paper presents a further improvement of the DME-PA-based near-infrared water vapour gas sensor. It uses the current modulation of near-infrared LEDs at two different frequencies *simultaneously*. This permits to excite both resonant modes of the DME-PA cell simultaneously and thus enables the determination of the amplitude ratio continuously without having to alternate the modulation frequency between the two resonant frequencies of the photoacoustic cell.

2 Experimental arrangement

The experimental arrangement is depicted in Fig. 1. The light source consists of an array of 4 InGaAsP near-infrared LEDs (Roithner LaserTechnik, model 1450-03) powered with a current driver (Thorlabs laser diode controller, model LDC500). The emitted light is collected and collimated into a parallel beam (diam. ca. 30 mm) with a glass (BK7) lens. The power of the collimated and modulated beam is ca. 3 mW, the near-infrared emission is centred at 1450 nm with a full width at half maximum (FWHM) of 100 nm. Figure 2 shows the LEDs emission spectrum and the water vapour absorption spectrum within the LEDs emission wavelength range. The forward current applied to the LEDs is modulated either with a single sine waveform or the sum of two sine waveforms having different frequencies. Modulation signals originate from two (respectively one, for the single-frequency excitation) lock-in amplifiers (Stanford Research Systems, model SR830), which also monitor the resulting photoacoustic signal at their respective modulation frequencies.

The photoacoustic cell consists of three cylinders (Fig. 1). The near-infrared excitation beam first hits the longest one (length 35 mm, diam. 30 mm). The outer part of the beam does not reach the second tube (length 30 mm, diam. 10 mm) while the rest propagates to the last tube (length 15 mm, diam. 30 mm). Both windows are made of borosilicate glass. An electret microphone (Knowles, model EK-3024) is placed in the middle of the central cylinder. The microphone signal is buffered and pre-amplified before being fed into the two lock-in amplifiers. Both photoacoustic signal amplitudes are then transmitted to a computer where the ratio of the photoacoustic signals at the two modulation frequencies is calculated.

Gaseous water vapour samples with different water content were prepared by continuously bubbling dried air through pure liquid water at $T = 293$ K. The resulting water-containing air-flow was then diluted with dried air using a mass-flow controller gas-mixing unit (Sierra, Serie800). Water contents of the generated gas samples are continuously monitored with a humidity meter (Vaisala, model HMI-31) calibrated with a dew point humidity meter (MBW Calibration, model 373L).

3 Results and discussion

Modulation-frequency scans of the photoacoustic responses for two different water concentrations (i.e. 0%vv and 2.1%vv) using a single excitation frequency (i.e. only one modulation frequency at a time) are presented in Fig. 3. The pressure in the photoacoustic cell was 980 mbar and the temperature 293 K. Two resonances are clearly visible with maxima at 4450 Hz and 5435 Hz.

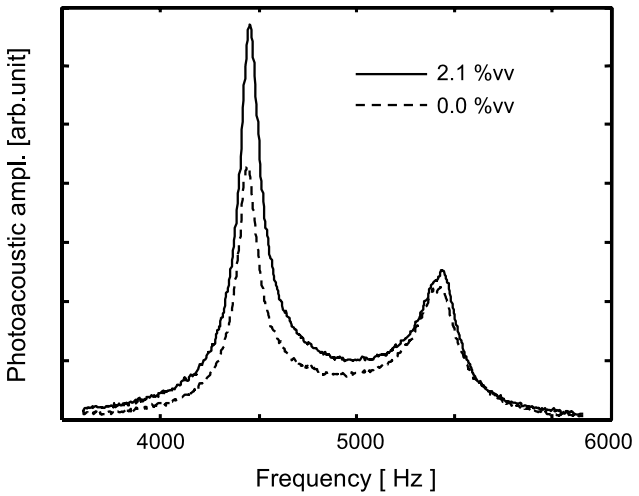

Fig. 3 Experimental frequency spectra of the photoacoustic cell for two different water vapour concentrations. The *dashed* and *full lines* show the photoacoustic amplitudes with 0.0%vv and 2.1%vv of water in the photoacoustic cell, respectively

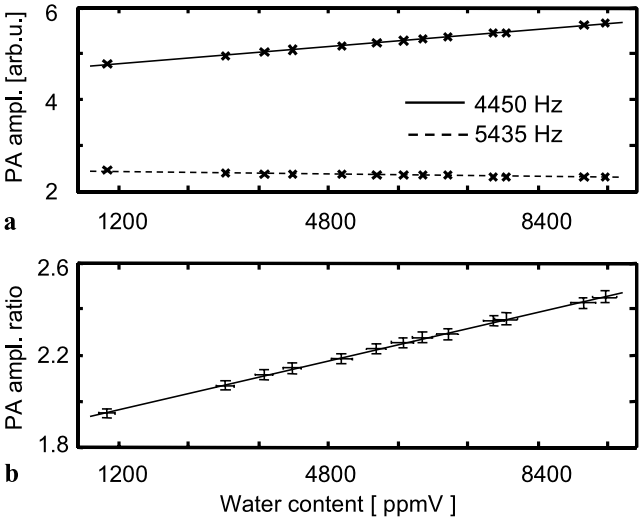

Fig. 4 Mode amplitudes and their ratio versus water vapour concentration. The full and dashed lines in part (**a**) are linear fits of the experimental photoacoustic amplitudes at the lower (i.e. 4450 Hz) and upper (i.e. 5435 Hz) resonance frequencies, respectively. Part (**b**) shows the corresponding experimental mode amplitude ratios, the *line* represents a linear fit. The *error bars* correspond to the $[-\sigma, +\sigma]$ ranges experimentally observed

Increasing the water content in the photoacoustic cell increases the photoacoustic amplitude of the low-frequency resonance and hardly affects the high-frequency one. This photoacoustic signal behaviour is explained using the extended Helmholtz resonator theory [21]. The central part of the light beam travels through the whole cell (Fig. 1) and generates a photoacoustic signal that mainly originates from the light absorbed inside the resonator. The outer part of the excitation light strikes the wall of the cell at the first tube constriction (i.e. between the first buffer volume and the resonator). This generates a signal originating from the first buffer volume and by absorption at the wall (at the cell constriction). The existence of a phase difference between the two photoacoustic modes in the first buffer volume and at the tube constriction explains the different behaviours of the two photoacoustic modes with increasing water concentration [21]. Since the two photoacoustic resonances are clearly separated, the maximum photoacoustic amplitude of a resonance is a measure of its mode amplitude.

Photoacoustic mode amplitudes for different water vapour content were measured using the simultaneous double-modulation scheme and represented by the $(\times)$ symbols in Fig. 4a. The larger photoacoustic signal amplitudes refer to the low-frequency resonance (4450 Hz, full line) whereas the smaller amplitudes correspond to the high frequency (5435 Hz, dashed line). The full and dashed lines represent linear fits (least square regression) of the experimental data points. The full line shows the linear behaviour of the low-frequency mode amplitude with increasing water content while the high-frequency one (dashed line) remains almost constant. Experimental mode amplitude ratios (i.e. the ratios between the photoacoustic signal amplitude of the lower to that of the higher resonance frequency) are given in Fig. 4b. This figure clearly demonstrates the linear correlation between the mode amplitude ratio and the water content of the photoacoustic cell. The corresponding noise level (1σ, 3.6 s acquisition time) represented by the vertical error bars is 0.95%. The dashed line in this figure is a linear fit (least square regression) of the experimental data points. Based on this linear fit and on the 1% amplitude noise, a measurement uncertainty of ± 330 ppmV (corresponding to $\pm 1.3\%$ relative humidity) is obtained.

A linear dependence of the photoacoustic signal amplitude with the intensity of the excitation light beam is observed (Fig. 5a) as expected for a photoacoustic sensor. Figure 5a shows both experimental mode amplitudes (i.e. mode amplitude at 4450 Hz and 5435 Hz) as a function of collimated LED light power. The mode amplitude ratio corresponding to the mode amplitudes shown in Fig. 5a is depicted in Fig. 5b. This figure implies that the variation of the mode amplitude ratio with the LED intensity is smaller than the experimental error, shown by the vertical error bars. The mode amplitude is thus independent on the LED intensity (i.e. no photoacoustic signal normalisation is required).

Typical experimental signal and noise figures for both sequential and simultaneous double-modulation frequency schemes are presented in Table 1. For a given excitation power reaching the photoacoustic cell and a given total acquisition time, the single modulation scheme leads to a stronger photoacoustic signal. However, in order to obtain the ratio of the photoacoustic amplitudes, the sequential (i.e. one-modulation at a time) scheme requires a change of modulation frequency since the photoacoustic amplitudes at both

Table 1 Typical photoacoustic amplitudes and their corresponding amplitude ratios for the sequential (one modulation frequency at a time) and simultaneous modulation schemes (see text). The total near-infrared light power reaching the photoacoustic cell is 2.9 mW. The photoacoustic cell was filled with 900 ppmV of water vapour

	Sequential modulation	Simultaneous modulation
Amplitude @ 4450 Hz [a.u.]	8.35	4.79
Amplitude @ 5435 Hz [a.u.]	4.29	2.46
Amplitude ratio	1.95	1.95
Ampl. Ratio noise level (σ/mean)		
acquisition time = 3.6 s	0.73%	0.95%
acquisition time = 15 s	0.58%	0.44%
Water content uncertainty ($\pm\sigma$) [ppmV]		
acquisition time = 3.6 s	$\pm$260	$\pm$330
acquisition time = 15 s	$\pm$205	$\pm$150

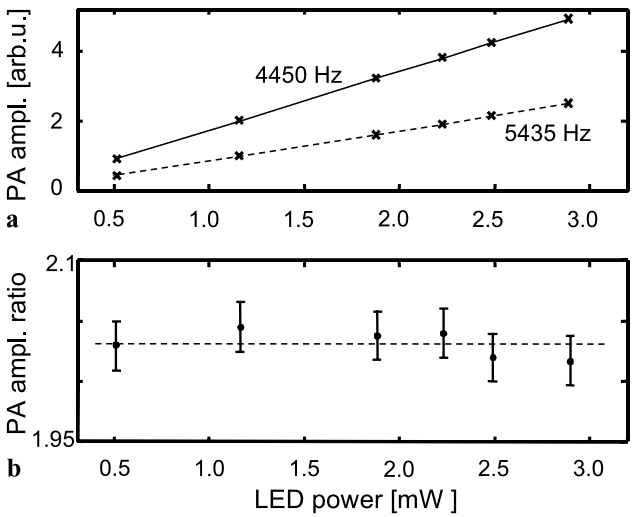

Fig. 5 Mode amplitudes and their ratio versus total LED power reaching the photoacoustic cell. The full and dashed lines in part (**a**) are linear fits of the experimental photoacoustic amplitudes at the lower (i.e. 4450 Hz) and upper (i.e. 5435 Hz) resonance frequencies, respectively. Part (**b**) shows the corresponding experimental mode amplitude ratios, the *line* represents a linear fit. The *error bars* indicate the $[-\sigma, +\sigma]$ ranges experimentally observed

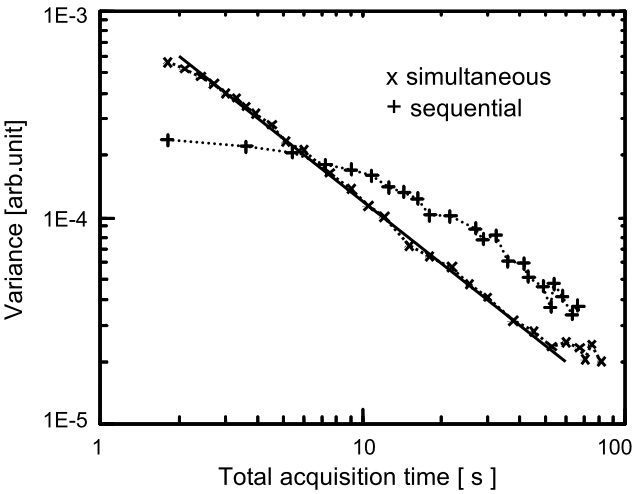

Fig. 6 Variance of the amplitude ratios versus total acquisition time. The ($\times$) and ($+$) symbols represent experimental results obtained with the simultaneous ($\times$) and sequential ($+$) modulation scheme, respectively. The *dotted lines* are guides for the eyes and the *full line* represents a line with slope $= -1$ (see text)

resonance frequencies are required. Changing the modulation frequency is a time-consuming step because the output filter used in the lock-in measurement technique requires time (i.e. at least 3 time constants of the low pass output filter) to reach a stable signal. For a given total light power reaching the photoacoustic cell, two times weaker photoacoustic amplitudes are obtained with the simultaneous double-modulation scheme since the whole excitation energy is split between the acoustic modes. Table 1 shows that for a short total acquisition time (3.6 s) the simultaneous modulation scheme has a worse noise figure than the sequential modulation scheme. However, when a total acquisition time of 15 s is employed, this drawback is clearly compensated by the longer averaging time available since no frequency change is needed. The variance of the amplitude ratio as function of the total acquisition time is presented in Fig. 6. This graph corresponds to an Allan-variance plot [22, 23], the horizontal axis being the total acquisition time and not only the lock-in time constant. A nearly linear behaviour is obtained (on the log-log plot, Fig. 6) for the variance with the simultaneous modulation scheme ($\times$ symbols). The full line exhibits a slope of -1. The good agreement for the slope between the experimental data ($\times$) and this line shows that the measurement is limited by white noise ($\sigma^2 \sim 1/\tau_{\text{acquisition}}$). The sequential scheme ($+$ symbols) shows a more complex behaviour; for a short total acquisition time the variance decreases slower than if only white noise was involved. This behaviour stems from the combination of short-term drifts and white noise affecting the se-

quential modulation scheme. For acquisition times shorter than 7 s, the sequential modulation scheme gives best results (Fig. 6) but the lowest measurement uncertainty is obtained with a long acquisition time using the simultaneous modulation scheme.

The main advantage of the DME-PA technique is the reduction of drifts caused by intensity fluctuations of the light source and microphone or electronics instabilities [24]. Since the drift compensation principle is linked to the use of photoacoustic amplitude ratios, it is thus only effective on a timescale longer than the one needed to obtain the photoacoustic amplitudes at both resonance frequencies. For the sequential modulation scheme, the ratio is obtained only at the end of the acquisition period. The simultaneous modulation scheme allows direct acquisition of the photoacoustic ratio and thus compensates for drifts during the acquisition period.

As listed in Table 1, a measurement uncertainty of ± 150 ppmV (corresponding to $\pm 0.6\%$ relative humidity) is obtained for an acquisition time of 15 s. This value is obviously orders of magnitude higher than the one obtained with laser-based devices [25–27]. This low sensitivity mainly comes from the modest match between the water absorption spectrum and the LED spectrum (Fig. 2). Nevertheless the near-infrared LED excitation source represents a much simpler (no power meter required) and cost-effective device than laser-based devices and still provides a $\pm 0.6\%$ relative humidity accuracy at room temperature and ambient pressure.

4 Conclusion

Results on the sequential and simultaneous excitation of two acoustic modes of a DME-PA system are presented. The main drawback of the sequential modulation scheme is the additional time required for changing the modulation frequency in order to obtain the amplitude ratio needed by the DME-PA technique. For a given excitation power reaching the photoacoustic cell and a total acquisition time of 3.6 s the sequential modulation scheme still shows a better noise figure than the simultaneous modulation scheme. Nevertheless with longer (>7 s) total acquisition time, the simultaneous modulation scheme provides an improved measurement uncertainty. Compared to the previous photoacoustic LED water vapour sensor [21] which operates with a sequential modulation scheme, the key advantage of the simultaneous LED excitation introduced in this work is to keep the advantages inherent to the DME-PA technique (i.e. reduced drifts due to intensity fluctuations of the light source and to microphone or electronics responses) also during the amplitude ratio acquisition time. The DME-PA sensor with simultaneous amplitude modulation allows measuring water vapour with a ± 150 ppmV ($\pm 1\sigma$) uncertainty using a simple current-modulated near-infrared LED and a 15 s total acquisition time. At the selected wavelength range no significant interference with the main air components (i.e. N_2, O_2, CO_2, CO, CH_4) occurs. Such a LED photoacoustic sensor could thus represent a valuable alternative to conventional capacitive or resistive humidity sensors with similar accuracy.

The sensitivity of the proposed DME-PA sensor can easily be improved by using a laser diode providing a better spectral match between the water absorption spectrum and the excitation light source. Since the DME-PA scheme with two simultaneous modulations is not restricted to the near-infrared, another way to improve the sensitivity is to take advantage of the higher mid-infrared absorption cross-section compared to the near-infrared ones by using mid-infrared LEDs [28] or lasers [29].

Acknowledgements The financial support by the ETH Zurich is greatly acknowledged. We thank D. Mutter from MBW Calibration Ltd for valuable suggestions about humidity measurements and for providing the dew point humidity calibrator.

References

1. T. Schmid, Anal. Bioanal. Chem. **384**, 1071 (2006)
2. A. Elia, P.M. Lugarà, C. Di Franco, V. Spagnolo, Sensors **9**, 9616 (2009)
3. A. Miklos, P. Hess, Z. Bozoki, Rev. Sci. Instrum. **72**, 1937 (2001)
4. V.P. Zharov, V.S. Letokhov, *Laser Optoacoustic Spectroscopy*. Springer Ser. Opt. Sci., vol. 37 (Springer, Berlin, 1986)
5. P. Hess, Top. Curr. Chem. **111**, 1 (1983)
6. R. Gerlach, N.H. Amer, Appl. Phys. **23**, 319 (1980)
7. A. Karbach, P. Hess, J. Chem. Phys. **84**, 2945 (1986)
8. C. Hornberger, M. König, S.B. Rai, W. Demtröder, Chem. Phys. **190**, 171 (1995)
9. F.G.C. Bijnen, F.J.M. Harren, J. Reuss, Rev. Sci. Instrum. **67**, 2914 (1996)
10. M. Mattiello, M. Nikles, S. Schilt, L. Thevenaz, A. Salhi, D. Barat, A. Vicet, Y. Rouillard, R. Wener, J. Koeth, Spectrochim. Acta A **63**, 952 (2006)
11. K.P. Koch, W. Lahmann, Appl. Phys. Lett. **32**, 289 (1978)
12. M. Nägele, M. W Sigrist, Appl. Phys. B **70**, 895 (2000)
13. F.J.M. Harren, F.G.C. Bijnen, J. Reuss, L.A.C.J. Voesenek, C.W.P.M. Blom, Appl. Phys. B **50**, 137 (1990)
14. F.J.M. Harren, R. Berkelmans, K. Kuiper, S. te Lintel Hekkert, P. Scheepers, R. Dekhuijzen, P. Hollander, D.H. Parker, Appl. Phys. Lett. **74**, 1761 (1999)
15. J.P. Besson, S. Schilt, E. Rochat, L. Thévenaz, Spectrochim. Acta A **63**, 899 (2006)
16. A. Miklos, A. Lorincz, Appl. Phys. B **48**, 213 (1989)
17. V. Zeninari, V.A. Kapitanov, D. Courtois, Y.N. Ponomarev, Infrared Phys. Technol. **40**, 1 (1999)
18. A.A. Kosterev, F.K. Tittel, D.V. Serebryakov, A.L. Malinovsky, I.V. Morozoy, Rev. Sci. Instrum. **76**, 043105 (2005)
19. J.M. Rey, M.W. Sigrist, Rev. Sci. Instrum. **78**, 063104 (2007)
20. J.M. Rey, M.W. Sigrist, Infrared Phys. Technol. **51**, 516 (2008)
21. J.M. Rey, M.W. Sigrist, Sens. Actuators B, Chem. **135**, 161 (2008)
22. D.W. Allan, Proc. IEEE **54**, 221 (1966)

23. P. Werle, R. Mücke, F. Slemr, Appl. Phys. B **57**, 131 (1993)
24. J.M. Rey, D. Marinov, D.E. Vogler, M.W. Sigrist, Appl. Phys. B **80**, 261 (2005)
25. L. Joly, V. Zeninari, B. Parvitte, D. Courtois, G. Durry, Opt. Lett. **31**, 143 (2006)
26. A. Beenen, R. Niessner, Analyst **123**, 543 (1998)
27. Z. Bozoki, M. Szakall, A. Mohacsi, G. Szabo, Z. Bora, Sens. Actuators B, Chem. **91**, 219 (2003)
28. N.V. Zotova, S.A. Karandashev, B.A. Matveev, M.A. Remenny, N.M. Stus, G.N. Talalakin, V.V. Shustov, Semiconductors **35**, 357 (2001)
29. I.T. Sorokina, K.L. Vodopyanov (eds.), *Solid-State Mid-Infrared Laser Sources*. Topics in Appl. Phys., vol. 89 (Springer, Berlin, 2003)
30. L.S. Rothman, D. Jacquemart, A. Barbe, D.C. Benner, M. Birk, L.R. Browne, M.R. Carleer, C. Chackerian, Jr., K. Chance, L.H. Coudert, V. Dana, V.M. Devi, J.M. Flaud, R.R. Gamache, A. Goldman, J.M. Hartmann, K.W. Jucks, A.G. Maki, J.Y. Mandin, S.T. Massie, J. Orphal, A. Perrin, C.P. Rinsland, M.A.H. Smith, J. Tennyson, R.N. Tolchenov, R.A. Toth, J. Vander Auwera, P. Varanasi, G. Wagner, J. Quant. Spectrosc. Rad. Transf. **96**, 139 (2005)